

Computational modeling of cardiac electrophysiology: A novel finite element approach

S. Göktepe and E. Kuhl^{*,†}

Departments of Mechanical Engineering and Bioengineering, Stanford University, Stanford, CA 94305, U.S.A.

SUMMARY

The key objective of this work is the design of an unconditionally stable, robust, efficient, modular, and easily expandable finite element-based simulation tool for cardiac electrophysiology. In contrast to existing formulations, we propose a global–local split of the system of equations in which the global variable is the fast action potential that is introduced as a nodal degree of freedom, whereas the local variable is the slow recovery variable introduced as an internal variable on the integration point level. Cell-specific excitation characteristics are thus strictly local and only affect the constitutive level. We illustrate the modular character of the model in terms of the FitzHugh–Nagumo model for oscillatory pacemaker cells and the Aliev–Panfilov model for non-oscillatory ventricular muscle cells. We apply an implicit Euler backward finite difference scheme for the temporal discretization and a finite element scheme for the spatial discretization. The resulting non-linear system of equations is solved with an incremental iterative Newton–Raphson solution procedure. Since this framework only introduces one single scalar-valued variable on the node level, it is extremely efficient, remarkably stable, and highly robust. The features of the general framework will be demonstrated by selected benchmark problems for cardiac physiology and a two-dimensional patient-specific cardiac excitation problem. Copyright © 2009 John Wiley & Sons, Ltd.

Received 22 July 2008; Revised 8 January 2009; Accepted 9 January 2009

KEY WORDS: cardiac physiology; finite element method; FitzHugh–Nagumo model; Aliev–Panfilov model; arrhythmia; spiral waves; re-entry

1. MOTIVATION

Heart disease is the primary cause of death in industrialized nations. In the United States, 10% of all deaths are suddenly caused by rhythm disturbances of the heart. In the healthy heart, cardiac

^{*}Correspondence to: E. Kuhl, Departments of Mechanical Engineering and Bioengineering, Stanford University, Stanford, CA 94305, U.S.A.

[†]E-mail: ekuhl@stanford.edu

Contract/grant sponsor: National Science Foundation; contract/grant number: EFRI-CBE 0735551

contraction is generated by smoothly propagating non-linear electrical waves of excitation. Disturbed conduction and uncoordinated electrical signals can generate abnormal heart rhythms, so-called arrhythmias. Typical examples of arrhythmias are bradycardia, tachycardia, heart block, re-entry, and atrial and ventricular fibrillation. Arrhythmias produce a broad range of symptoms from barely noticeable to cardiovascular collapse, cardiac arrest and death [1–7]. The excitation of cardiac cells is initiated by a sudden change in the electrical potential across the cell membrane due to the transmembrane flux of charged ions. The initiation and propagation of an electrical signal by controlled opening and closing of ion channels are one of the most important cellular functions. Its first quantitative model was proposed more than half a century ago by Hodgkin and Huxley [8] for cells of a squid axon. In their pioneering model, based on the circuit analogy, Figure 2 (right), the local evolution of an action potential Φ is described by the differential equation $C_m \dot{\Phi} + I_{\text{ion}} = I_{\text{app}}$ where C_m stands for the membrane capacitance per unit area and I_{ion} , I_{app} denote the sum of the ionic currents and the externally applied current, respectively. For a squid axon, the total ionic transmembrane current is chiefly due to the sodium current I_{Na} and the potassium current I_{K} ; that is, $I_{\text{ion}} = I_{\text{Na}} + I_{\text{K}} + I_{\text{L}}$. The additional *leakage* current I_{L} is introduced to account for the other small ionic currents in a lumped form. The current due to the flow of an individual ion is modeled by the ohmic law $I_{\alpha} = g_{\alpha}(\Phi - \Phi_{\alpha})$, where $g_{\alpha} = \hat{g}_{\alpha}(t; \Phi)$ denotes the voltage- and time-dependent conductance of the membrane to each ion and Φ_{α} are the corresponding equilibrium (Nernst) potentials for $\alpha = \text{Na}, \text{K}, \text{L}$. The potassium conductance is assumed to be described by $g_{\text{K}} = \bar{g}_{\text{K}} n^4$ where n is called the potassium activation and \bar{g}_{K} is the maximum potassium conductance. The sodium conductance, however, is considered to be given by $g_{\text{Na}} = \bar{g}_{\text{Na}} m^3 h$ with \bar{g}_{Na} being the maximum sodium conductance, m the sodium activation, and h the sodium inactivation. Temporal evolution of the gating variables m , n , and h is then modeled by first-order differential equations whose rate coefficients are also voltage dependent. The diagram in Figure 1 (left) depicts the action potential calculated with the original Hodgkin–Huxley model. The action potential that favorably agrees with their experimental measurements possesses the four characteristic upstroke, excited, refractory, and recovery phases. The time evolution of the three gating variables shown in Figure 1 (right) illustrates dynamics of the distinct activation and inactivation mechanisms. Although their theory had originally been developed for neurons, it was soon modified and generalized to explain a wide variety of excitable cells. The original Hodgkin–Huxley model was significantly simplified by FitzHugh [9] who introduced an extremely elegant two-parameter formulation that allowed the rigorous analysis of the underlying action potentials with well-established mathematical tools. It is formulated in terms of the fast action potential and a slow recovery variable that phenomenologically summarizes the effects of all ionic currents in one single variable.

Action potentials occur when the cell membrane depolarizes and then repolarizes back to the steady state. There are two conceptually different action potentials in the heart: action potentials for pacemaker cells such as the sinoatrial and the atrioventricular node, and action potentials for non-pacemaker cells such as atrial or ventricular muscle cells. For example, the diagrams in Figure 5 depict the representative action potentials for the atrioventricular node and the non-pacemaker cardiac muscle along with physiologically relevant time scales. Pacemaker cells are capable of spontaneous action potential generation, whereas non-pacemaker cells have to be triggered by depolarizing currents from adjacent cells. The main difference between a pacemaker cell and a cardiac muscle cell is the presence of calcium that regulates contractile function. The first model describing the action potential of cardiac cells was proposed by Noble [10] for Purkinje fiber cells. Beeler and Reuter [11] introduced the first mathematical model for ventricular myocardial cells,

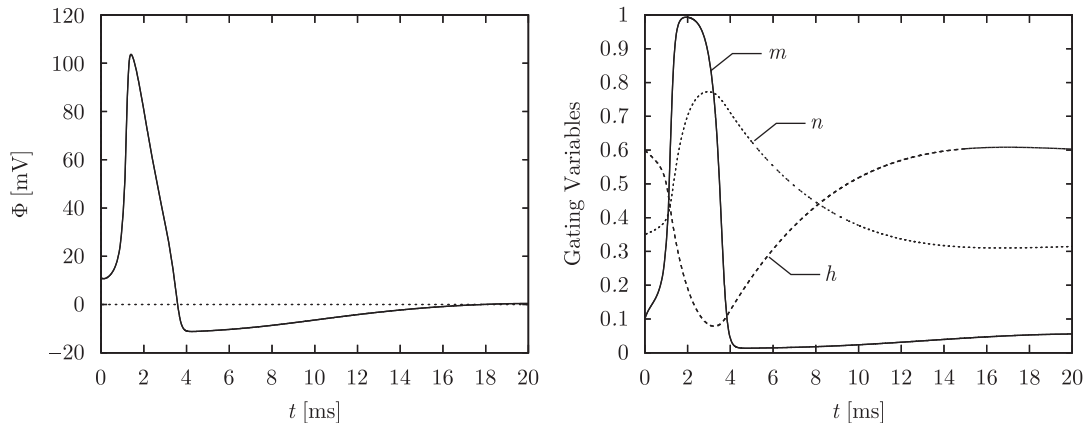


Figure 1. Action potential calculated with the original Hodgkin–Huxley model (left). Evolution of the corresponding gating variables m , n , and h during the action potential (right).

which was modified through enhanced calcium kinetics by Luo and Rudy [12]. The recent literature provides excellent classifications of these and more sophisticated cardiac cell models [13–17].

About a decade ago, Aliev and Panfilov [18] and Fenton and Karma [19] suggested the numerical analysis of traveling excitation waves with the help of explicit finite difference schemes. At the same time, one of the first finite element algorithms for cardiac action potential propagation was proposed by Rogers and McCulloch [20–22]. They suggested combined Hermitian/Lagrangian interpolation for the unknowns. Recent attempts aim at incorporating the mechanical field through excitation–contraction coupling. The physiology of the underlying coupling mechanisms is explained in detail by Hunter *et al.* [23]. Existing computational excitation–contraction coupling algorithms are based on a staggered solution that combines a finite difference approach to integrate the excitation equations through an explicit Euler forward algorithm with a finite element approach for the mechanical equilibrium problem [24–28]. Accordingly, they require sophisticated mappings from a fine electrical grid to a coarse mechanical mesh to map the potential field and vice versa to map the deformation field. It is also worth mentioning that the motion of an excitation wavefront can be approximated by *Eikonal* equations. This approach solely focusses on the motion of the depolarization wavefront and seeks for the excitation time as a field. Hence, it reduces the complete equations of excitation dynamics to a problem of wavefront propagation thereby often suppresses time dependency [13, 29]. Although the approaches based on the Eikonal equations have been considered to be useful for fast qualitative computation of depolarization wavefront propagation, they lack the precise description of the phenomena, which is crucial for the coupled excitation–contraction problem.

Through a novel finite element algorithm for the excitation problem, this paper lays the groundwork for a fully coupled monolithic finite element framework for excitation–contraction coupling. It is organized as follows: After a brief summary of the governing equations of electrophysiology in Section 2, we will illustrate their novel single degree of freedom finite element formulation in Section 3. The constitutive equations that specify the characteristic action potentials of different cells and govern their spatial propagation are discussed in Section 4. In particular, Section 4.1 illustrates oscillatory pacemaker cells, and Section 4.2 describes non-oscillatory cardiac muscle

cells. Section 5 demonstrates the features of the suggested finite element algorithm by means of common phenomena of arrhythmogenesis. Finally, Section 6 concludes with a critical discussion of model limitations and potential further research directions.

2. GOVERNING EQUATIONS OF ELECTROPHYSIOLOGY

In this section, we summarize the governing equations of electrophysiology motivated by the classical FitzHugh–Nagumo model. The FitzHugh–Nagumo model extracts the essential characteristics of the Hodgkin–Huxley model and summarizes its information in terms of one-fast and one-slow variable. It was FitzHugh who was the first to observe that the original four-variable Hodgkin–Huxley model can be approximated to a two-variable model. Based on the temporal evolution of gating variables of the Hodgkin–Huxley model, depicted in Figure 1 (right), he observed that the sodium activation m evolves fast and is almost in-phase with the action potential, whereas the sodium inactivation h and the potassium activation n change with considerable retardation. His second rightful observation is related with the symmetric evolution of n and h , i.e. their approximately constant sum $n+h \approx C$ (see also Keener and Sneyd [13, p. 133]). The two observations result in the reduced Hodgkin–Huxley model that involves only two evolution equations: one for the fast variable Φ and another one for a slow variable either n or h without sacrificing main characteristics of the original model. This simplification has also opened up the possibilities to analyze the reduced two variable, fast-slow system in the phase plane, and thereby the interpretation of the underlying characteristics of the model and its extension to more general phenomenological models. Mathematically speaking, the evolution equations of these two variables can be motivated by oscillations ϕ characterized through the following linear second-order equation:

$$\ddot{\phi} + k\dot{\phi} + \phi = 0 \quad (1)$$

Van der Pol [30] suggested replacing the constant damping coefficient k with a quadratic term in terms of the potential $k = c[\phi^2 - 1]$ to obtain the following non-linear equation:

$$\ddot{\phi} + c[\phi^2 - 1]\dot{\phi} + \phi = 0 \quad (2)$$

With the help of Liénard's transformation with $y = -\dot{\phi}/c - \phi^3/3 + \phi$, this second-order equation can be transformed into a system of two first-order equations

$$\dot{\phi} = c \left[-\frac{1}{3}\phi^3 + \phi + r \right], \quad \dot{r} = -\frac{1}{c}\phi \quad (3)$$

Its fast variable ϕ , the potential, has a cubic non-linearity allowing for regenerative self-excitation through a fast positive feedback. The slow variable r , the recovery variable, has a linear dynamics providing slow negative feedback. By adding a stimulus I and two additional terms a and br , FitzHugh [9] modified the above set of equations to what he referred to as the Bonhoeffer–van-der-Pol model

$$\dot{\phi} = c \left[-\frac{1}{3}\phi^3 + \phi + r + I \right], \quad \dot{r} = -\frac{1}{c}[\phi + br - a] \quad (4)$$

Today, the above equations are referred to as FitzHugh–Nagumo equations. Nagumo *et al.* [31] contributed essentially to their understanding by building the corresponding circuit to model the

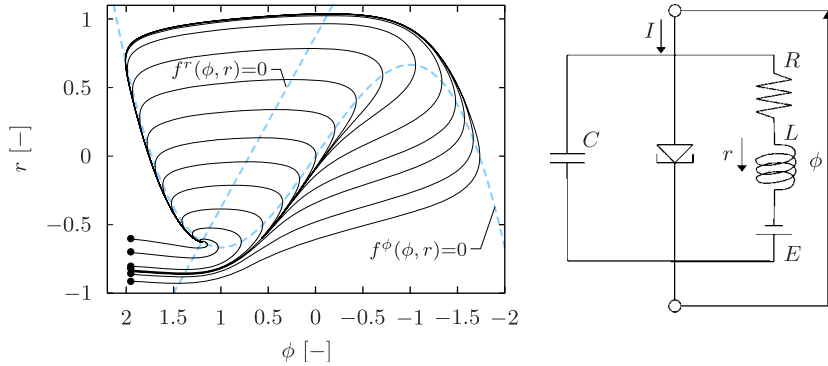


Figure 2. Phase portrait of classical FitzHugh–Nagumo model with $a=0.7$, $b=0.8$, $c=3$ (left). Trajectories for the distinct initial values of non-dimensional potential ϕ_0 and recovery variable r_0 (filled circles) converge to steady state. Dashed lines denote nullclines with $f^\phi=0$ and $f^r=0$. Circuit diagram of corresponding tunnel-diode nerve model (right).

cell through a capacitor for the membrane capacitance, a non-linear current–voltage device for the fast current and a resistor, an inductor and a battery in series for the recovery current, see Figure 2 (right). Being restricted to only two degrees of freedom, the FitzHugh–Nagumo model can be analyzed and interpreted in the two-dimensional phase space as illustrated in Figure 2 (left). The dashed lines represent the two nullclines for $r = \frac{1}{3}\phi^3 - \phi$ for $\dot{\phi} = 0$ and $r = [a - \phi]/b$ for $\dot{r} = 0$, respectively. The nullclines are assumed to have a single intersection point that represents the steady state of equilibrium at which $\dot{\phi} = 0$ and $\dot{r} = 0$. For low external stimuli I , this equilibrium point is stable, as shown in Figure 2. It is located at the left of the local minimum of the cubic nullcline, and all trajectories ultimately run into this stable equilibrium point. An increase of the external stimulus I shifts the cubic nullcline upwards. This causes the equilibrium point to move to the right. For sufficiently large stimuli, the steady state is located on the unstable middle branch of the cubic nullcline, and the model exhibits periodic activity referred to as tonic spiking. The FitzHugh–Nagumo system is said to be excitable: A sufficiently large perturbation from the steady state sends the state variables on a trajectory that initially runs away from equilibrium before returning to the steady state. This excitation is characterized through four phases: (i) the regenerative phase with a fast increase of the membrane potential ϕ ; (ii) the active phase with a high and almost constant membrane potential ϕ causing a slow increase of the recovery variable r ; (iii) the absolutely refractory phase with a fast decrease of the membrane potential ϕ at almost constant recovery r ; and (iv) the relatively refractory phase with a slow decrease of the recovery variable r as the solution slowly returns to the equilibrium point. Based on the above considerations, we will now derive a finite element formulation for excitable cardiac tissue characterized through the generalized FitzHugh–Nagumo equations stated in the following form:

$$\begin{aligned} \dot{\phi} &= \text{div } \mathbf{q}(\phi) + f^\phi(\phi, r) \\ \dot{r} &= f^r(\phi, r) \end{aligned} \quad (5)$$

The right-hand sides have been collectively summarized in two source terms $f^\phi(\phi, r)$ and $f^r(\phi, r)$. To account for the nature of traveling waves in excitable media, a phenomenological diffusion term $\text{div } \mathbf{q}(\phi)$ has been added to the original local version of the FitzHugh–Nagumo equations.

In the general case of anisotropic diffusion, the potential flux \mathbf{q} and its derivative $d_{\nabla\phi}\mathbf{q}$ can be expressed in the following phenomenological form:

$$\mathbf{q} = \mathbf{D} \cdot \nabla \phi, \quad d_{\nabla\phi}\mathbf{q} = \mathbf{D} \quad (6)$$

Here, $\mathbf{D} = d^{\text{iso}}\mathbf{I} + d^{\text{ani}}\mathbf{n} \otimes \mathbf{n}$ denotes the conductivity tensor, which consists of an isotropic and an anisotropic contribution d^{iso} and d^{ani} whereby the latter is weighted with the structural tensor of the direction of anisotropy, e.g. the myocardial fiber direction. Typical conductivities in cardiac tissue are 0.05 m/s for the sinoatrial and the atrioventricular node, 1 m/s for the atrial pathways, the bundle of His and the ventricular muscle, and 4 m/s for the Purkinje system, see, e.g. Ganong [1]. Based on the assumption that the spatial range of the signaling phenomenon ϕ is significantly larger than the influence domain of the recovery variable r , Equation (5)₂ is considered to be strictly local. This assumption is essential for the finite element formulation derived in the sequel.

3. FINITE ELEMENT FORMULATION OF ELECTROPHYSIOLOGY

Owing to the global nature of the cubic equation for the fast variable (5)₁ induced through its diffusion term, a \mathcal{C}^0 -continuous finite element interpolation is applied for the membrane potential ϕ . The recovery equation (5)₂, however, is strictly local. It is thus sufficient to interpolate the recovery variable r in a \mathcal{C}^{-1} -continuous way. Accordingly, the membrane potential is introduced as global degree of freedom on each finite element node, whereas the recovery variable treated as an internal variable to be stored locally at the integration point level. The finite element formulation for electrophysiology is derived from the strong form of the non-linear excitation equation (5)₁, which is cast into the following residual statement:

$$\mathbf{R}^\phi = \dot{\phi} - \text{div}(\mathbf{q}) - f^\phi \doteq 0 \quad \text{in } \mathcal{B} \quad (7)$$

The boundary $\partial\mathcal{B}$ of the domain \mathcal{B} can be decomposed into disjoint parts $\partial\mathcal{B}_\phi$ and $\partial\mathcal{B}_q$. Dirichlet boundary conditions are prescribed as $\phi = \bar{\phi}$ on $\partial\mathcal{B}_\phi$. Neumann boundary conditions can be given for the flux $\mathbf{q} \cdot \mathbf{n} = \bar{q}$ on $\partial\mathcal{B}_q$ with \mathbf{n} denoting the outward normal to $\partial\mathcal{B}$. Primarily homogeneous Neumann boundary conditions have been applied in the literature. The residual statement (7) and the corresponding Neumann boundary conditions are integrated over the domain, tested by the scalar-valued test function $\delta\phi$, and modified with the help of an integration by parts and Gauss' theorem to render the following weak form as:

$$\mathbf{G}^\phi = \int_{\mathcal{B}} \delta\phi \dot{\phi} dV + \int_{\mathcal{B}} \nabla\delta\phi \cdot \mathbf{q} dV - \int_{\partial\mathcal{B}_q} \delta\phi \bar{q} dA - \int_{\mathcal{B}} \delta\phi f^\phi dV = 0 \quad (8)$$

which is required to vanish $\forall \delta\phi \in H_1^0(\mathcal{B})$. For the spatial discretization, the domain of interest \mathcal{B} is discretized with n_{el} elements \mathcal{B}^e as $\mathcal{B} = \bigcup_{e=1}^{n_{\text{el}}} \mathcal{B}^e$. According to the isoparametric concept, the trial functions $\phi^h \in H_1(\mathcal{B})$ are interpolated on the element level with the same shape function N as the test functions $\delta\phi^h \in H_1^0(\mathcal{B})$. Here, $i, j = 1, \dots, n_{\text{en}}$ denote the n_{en} element nodes

$$\delta\phi^h|_{\mathcal{B}^e} = \sum_{i=1}^{n_{\text{en}}} N^i \delta\phi_i, \quad \phi^h|_{\mathcal{B}^e} = \sum_{j=1}^{n_{\text{en}}} N^j \phi_j \quad (9)$$

For the temporal discretization, the time interval of interest \mathcal{T} is partitioned into n_{stp} subintervals $[t_n, t_{n+1}]$ as $\mathcal{T} = \bigcup_{n=0}^{n_{\text{stp}}-1} [t_n, t_{n+1}]$. The time increment of the current time slab $[t_n, t_{n+1}]$ is denoted as $\Delta t := t_{n+1} - t_n > 0$. The nodal degrees of freedom ϕ_n and all derivable quantities are assumed to be known at the beginning of the actual subinterval t_n . To solve for the unknown potential ϕ at time t_{n+1} , we apply the classical Euler backward time integration scheme, in combination with the following finite difference approximation of the first-order material time derivative

$$\dot{\phi} = [\phi - \phi_n] / \Delta t \quad (10)$$

With the spatial and temporal discretizations (9) and (10), the discrete algorithmic residual \mathbf{R}_I^ϕ follows straightforwardly from the weak form (8)

$$\mathbf{R}_I^\phi = \mathbf{A} \int_{\mathcal{B}^e} N^i \frac{\phi - \phi_n}{\Delta t} + \nabla N^i \cdot \mathbf{q} \, dV - \int_{\partial \mathcal{B}_q^e} N^i \bar{q} \, dA - \int_{\mathcal{B}^e} N^i f^\phi \, dV \doteq 0 \quad (11)$$

Note that the index $(\cdot)_{n+1}$ has been omitted for the sake of clarity. The operator \mathbf{A} symbolizes the assembly of all element contributions at the element nodes $i = 1, \dots, n_{\text{en}}$ to the overall residual at the global node points $I = 1, \dots, n_{\text{nd}}$. Since the residual is a highly non-linear function in terms of the membrane potential we apply an incremental iterative Newton–Raphson solution strategy based on the consistent linearization of the governing equations at time t_{n+1} introducing the following global symmetric iteration matrix:

$$\partial_{\phi_j} \mathbf{R}_I^\phi = \mathbf{A} \int_{\mathcal{B}^e} N^i \frac{1}{\Delta t} N^j + \nabla N^i \cdot \mathbf{d}_{\nabla \phi} \mathbf{q} \cdot \nabla N^j - N^i \mathbf{d}_\phi f^\phi N^j \, dV \quad (12)$$

The iterative update for the increments of the global unknowns $\Delta \phi_I$ then follows straightforwardly in terms of the inverse of the iteration matrix $\partial_{\phi_j} \mathbf{R}_I^\phi$ from Equation (12) and the global right-hand side vector \mathbf{R}_J^ϕ from Equation (7)

$$\Delta \phi_I \leftarrow \Delta \phi_I - \sum_{J=1}^{n_{\text{nd}}} [\partial_{\phi_j} \mathbf{R}_I^\phi]^{-1} \mathbf{R}_J^\phi \quad \forall I = 1, \dots, n_{\text{nd}} \quad (13)$$

In what follows, we shall specify the traveling signal through the flux vector \mathbf{q} , the total transmembrane current f^ϕ , the source term f^r , and their linearizations $\mathbf{d}_{\nabla \phi} \mathbf{q}$ and $\mathbf{d}_\phi f^\phi$ required to evaluate the global residual (11) and the global iteration matrix (12).

4. CONSTITUTIVE EQUATIONS OF ELECTROPHYSIOLOGY

In this section, we specify the constitutive equations for the source terms f^ϕ and f^r for distinct cell types. Since the shape of the action potential can be quite different for different cell types, we will now discuss the choice of the source terms f^ϕ and f^r for oscillatory pacemaker cells and for non-oscillatory heart muscle cells and illustrate their individual excitation characteristics.

4.1. The generalized FitzHugh–Nagumo model for oscillatory pacemaker cells

Rhythmically discharging cells, such as the sinoatrial node, the atrioventricular node, and, under some conditions also the Purkinje fibers, have a membrane potential that, after each impulse,

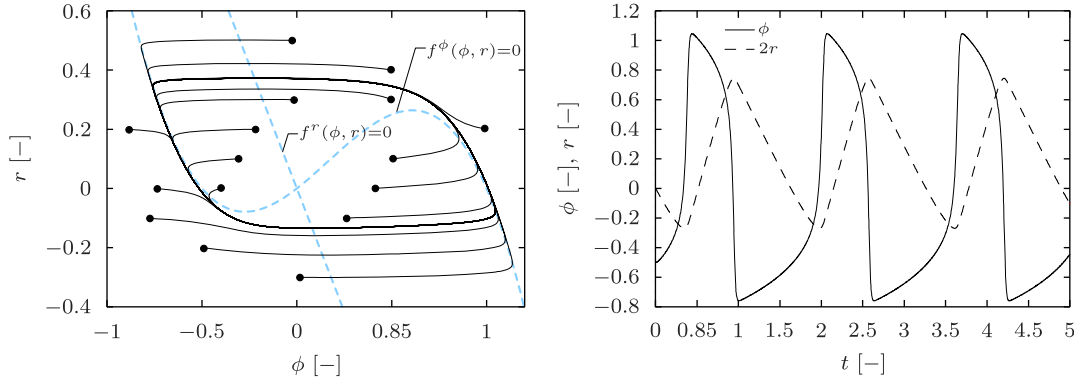


Figure 3. The generalized FitzHugh–Nagumo model with $\alpha=-0.5$, $a=0$, $b=-0.6$, $c=50$. The phase portrait depicts the trajectories for distinct initial values of non-dimensional potential ϕ_0 and recovery variable r_0 (filled circles) converge to a stable limiting cycle. Dashed lines denote nullclines with $f^\phi=0$ and $f^r=0$ (left). Self-oscillatory time plot of the non-dimensional action potential ϕ and the recovery variable r (right).

declines to the firing level. The existence of a prepotential, which triggers the next impulse is characteristic for pacemaker cells. Mathematically, spontaneous activation is characterized through an unstable equilibrium state that manifests itself in an oscillatory response. We can rewrite the classical FitzHugh–Nagumo equation (4)

$$f^\phi = c[\phi(\phi - \alpha)[1 - \phi] - r] \tag{14}$$

in terms of the oscillation threshold α . For negative thresholds, $\alpha < 0$, the intersection of the nullclines is located in the unstable regime, i.e. between the two local extrema, see Figure 3 (left). In the phase diagram, all initial points run into an oscillatory path and then keep oscillating. In the time plot of Figure 3 (right), the membrane potential clearly displays the typical pacemaker function: The fast and slow variable undergo an oscillation through the four-phase cycle of the regenerative, the active, the absolutely refractory, and the relatively refractory phase. After this cycle, the membrane potential is above the critical threshold to initiate a new excitation cycle. With the source term for the recovery variable

$$f^r = \phi - br + a \tag{15}$$

combined with an implicit Euler backward integration, and a finite difference approximation $\dot{r} = [r - r_n]/\Delta t$ in time, the recovery variable r at t_{n+1} can be expressed as follows:

$$r = \frac{r_n + [\phi + a]\Delta t}{1 + b\Delta t} \tag{16}$$

To complete the constitutive equations, the total derivative $d_\phi f^\phi = \partial_\phi f^\phi + \partial_r f^\phi d_\phi r$ of Equation (14)

$$d_\phi f^\phi = c[-3\phi^2 + 2[1 - \alpha]\phi - \alpha] - \frac{c\Delta t}{1 + b\Delta t} \tag{17}$$

needs to be determined locally and passed to the element level where it enters the global Newton iteration (12).

Remark 1

Conversion of the non-dimensional action potential ϕ and time t of the generalized FitzHugh–Nagumo model to their physiological counterparts Φ (mV) and τ (ms) is carried out through

$$\Phi^{\text{fhn}} = [65\phi - 35] \text{ mV} \quad \text{and} \quad \tau^{\text{fhn}} = [220t] \text{ ms} \quad (18)$$

respectively. For comparison, the reader is referred to the diagrams in Figure 3 (right) and Figure 5 (left).

4.2. The Aliev–Panfilov model for non-oscillatory cardiac muscle cells

Unlike pacemakers cells that are primarily responsible to transmit the electrical signal, atrial and ventricular muscle cells are both excitable and contractile; however, they are typically not spontaneously contracting. The action potential of cardiac muscle cells is characterized through a sharp upstroke followed by an elongated plateau facilitating muscular contraction. The Aliev–Panfilov model [18] is maybe the most elegant model that captures the characteristic action potential of ventricular cells in a phenomenological sense through only two parameters. Its membrane potential ϕ is governed by the following source term:

$$f^\phi = c\phi[\phi - \alpha][1 - \phi] - r\phi \quad (19)$$

In contrast to the original FitzHugh–Nagumo model, the last term in the recovery variable r has been scaled by the membrane potential ϕ to avoid hyperpolarization. The evolution of the recovery variable is driven by the following source term:

$$f^r = \left[\gamma + \frac{\mu_1 r}{\mu_2 + \phi} \right] [-r - c\phi[\phi - b - 1]] \quad (20)$$

An additional non-linearity has been introduced through the weighting factor $[\gamma + \mu_1 r / \mu_2 + \phi]$ which allows to tune the restitution curve phenomenologically with respect to the experimental observations by adjusting the parameters μ_1 and μ_2 . In the phase diagram, arbitrary perturbations away from the steady state run into the stable equilibrium point, see Figure 4 (left). In the time plot, both the membrane potential and the recovery variable converge to a constant equilibrium value, see Figure 4 (right). Again, we suggest to treat the recovery r as internal variable and store its value locally on the integration point level. However, due to the additional non-linearity, its update can no longer be expressed explicitly. We suggest a local Newton iteration to solve the following residual expression:

$$\mathbf{R}^r = r - r_n - \left[\left[\gamma + \frac{\mu_1 r}{\mu_2 + \phi} \right] [-r - c\phi[\phi - b - 1]] \right] \Delta t \doteq 0 \quad (21)$$

Similar to the FitzHugh–Nagumo model, we have applied an implicit Euler backward time-stepping scheme in combination with the finite difference interpolation $\dot{r} = [r - r_n] / \Delta t$. The above residual and its linearization

$$\partial_r \mathbf{R}^r = 1 + \left[\gamma + \frac{\mu_1}{\mu_2 + \phi} [2r + c\phi[\phi - b - 1]] \right] \Delta t \quad (22)$$

define the incremental update of the recovery variable as $r \leftarrow r - [\partial_r \mathbf{R}^r]^{-1} \mathbf{R}^r$. For the total derivative $d_\phi f^\phi = \partial_\phi f^\phi + \partial_r f^\phi d_\phi r$ required for the global Newton iteration (12) we need to determine

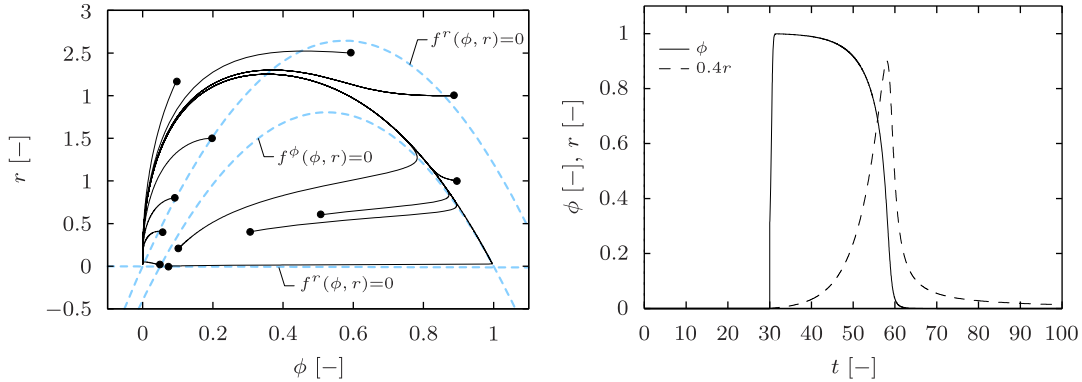


Figure 4. The Aliev–Panfilov model with $\alpha=0.05$, $\gamma=0.002$, $b=0.15$, $c=8$, $\mu_1=0.2$, $\mu_2=0.3$. The phase portrait trajectories for distinct initial values of non-dimensional potential ϕ_0 and recovery variable r_0 (filled circles) converge to stable equilibrium point. Dashed lines denote nullclines with $f^\phi=0$ and $f^r=0$ (left). Non-oscillatory time plot of the non-dimensional action potential ϕ and the recovery variable r is triggered by external stimulation $I=30$ from the steady state $\phi_0=r_0=0$ (right).

Table I. Local Newton iteration to update internal variable r and determine corresponding source term f^ϕ and its linearization $d_\phi f^\phi$.

-
- given ϕ_n , r_n , and ϕ
 - i) let $r \leftarrow r_n$
 - ii) compute \mathbf{R}^r from (21) and $\partial_r \mathbf{R}^r$ from (22)
 - iii) update recovery $r \leftarrow r - [\partial_r \mathbf{R}^r]^{-1} \mathbf{R}^r$
 - iv) check $|r| < \text{tol}$, if no goto ii), yes continue
 - v) compute $\partial_\phi \mathbf{R}^r$ from (24) and $d_\phi r$ from (23)
 - vi) compute f^ϕ from (19) and $d_\phi f^\phi$ from (25)
 - vii) update history for r_n
-

the derivative of the recovery variable $d_\phi r$. This derivative can be evaluated at local equilibrium $d_\phi \mathbf{R}^r = \partial_\phi \mathbf{R}^r + \partial_r \mathbf{R}^r d_\phi r \doteq 0$ as

$$d_\phi r = -[\partial_r \mathbf{R}^r]^{-1} \partial_\phi \mathbf{R}^r \quad (23)$$

with

$$\partial_\phi \mathbf{R}^r = \left[\left[\gamma + \frac{\mu_1 r}{\mu_2 + \phi} \right] c [2\phi - b - 1] - \frac{\mu_1 r}{[\mu_2 + \phi]^2} [r + c\phi[\phi - b - 1]] \right] \Delta t \quad (24)$$

and $\partial_r \mathbf{R}^r$ given in Equation (22). The total derivative for the global Newton iteration (12) can then be expressed as follows:

$$d_\phi f^\phi = c[-3\phi^2 + 2[1 - \alpha]\phi + \alpha] - r - \phi d_\phi r \quad (25)$$

Table I summarizes the local Newton iteration to update the internal variable r and determine the corresponding source term f^ϕ and its linearization $d_\phi f^\phi$.

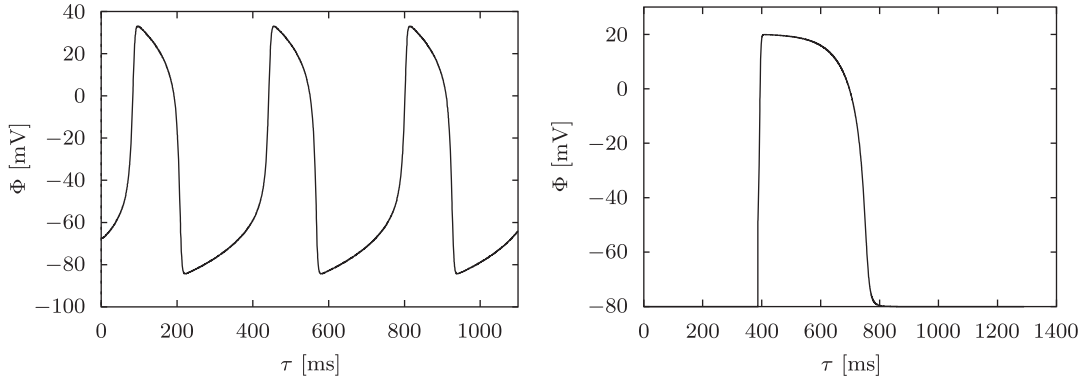


Figure 5. Physiological action potential-time plots corresponding to the generalized FitzHugh–Nagumo model (left) and the Aliev–Panfilov model (right). Physiologically relevant Φ (mV) and time τ (ms) values of the respective models are obtained by using the conversion formulas given in (18) and (26).

Remark 2

Conversion of the non-dimensional action potential ϕ and time t of the generalized Aliev–Panfilov model to their physiological counterparts Φ (mV) and τ (ms) is carried out through

$$\Phi^{\text{ap}} = [100\phi - 80] \text{mV} \quad \text{and} \quad \tau^{\text{ap}} = [12.9t] \text{ms} \quad (26)$$

respectively. For comparison, the reader is referred to the diagrams in Figure 4 (right) and Figure 5 (right).

5. ILLUSTRATIVE EXAMPLES

This section is devoted to the representative numerical examples that aim to illustrate the features of the proposed novel excitation algorithm. After validating the model in terms of the local restitution curve for the Aliev–Panfilov model in Section 5.1, we illustrate the global performance of the model by means of finite element analyses of initial boundary-value problems. The first set of examples in Section 5.2 is concerned with heterogeneously structured cardiac tissue. We explore the interaction of single and multiple pacemaker cells with non-oscillating cardiac muscle cells possessing either isotropic or anisotropic conduction properties. The subsequent example in Section 5.3 addresses the mechanism of initiation, development, and rotation of spiral waves in cardiac muscle tissue. In the last example in Section 5.4, we analyze excitation of the human heart based on a patient-specific dissection with a detailed cardiac conduction system to demonstrate that the proposed algorithm is capable of predicting physiologically correct excitation times. In all initial boundary-value problems, conversion of the non-dimensional action potential ϕ and time t of the both models to their physiological counterparts Φ (mV) and τ (ms) is carried out through the formulas (18) and (26) outlined in Remarks 1 and 2, respectively.

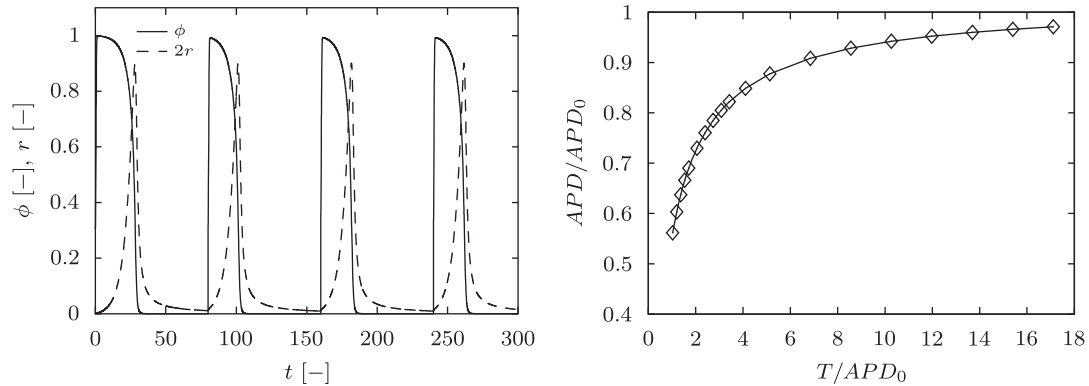


Figure 6. Restitutive response of Aliev–Panfilov model. Non-dimensional action potential ϕ and recovery variable r for $\alpha=0.05$, $\gamma=0.002$, $b=0.15$, $c=8$ excited by cyclic external stimulation with $I=30$ over time period $T=80[-]$ (left). Frequency-dependent normalized duration of action potential APD/APD_0 plotted against normalized period of stimulation T/APD_0 (right).

5.1. Restitution of cardiac tissue

To validate our model, we first compute the local restitution curve for cardiac muscle tissue and compare the results with the existing literature [18, 24]. A restitution curve of cardiac tissue depicts the dependence of the action potential duration on the period T of the stimulation I (see Figure 6). It is physiologically well known that the duration of the action potential of the myocardium considerably shortens as the frequency $1/T$ of the stimulation is increased [18, 24]. This shortening can have devastating physiological consequences and initiate cardiac arrhythmia upon the abrupt increase of the heart rate. In contrast to the FitzHugh–Nagumo model, the Aliev–Panfilov model accounts for the restitution property of cardiac muscle through the non-linear factor $[\gamma + \mu_1 r / (\mu_2 + \phi)]$ on the right-hand side of Equation (19). The shape of the restitution curve is governed by the phenomenological parameters μ_1 and μ_2 . In order to show the restitutive feature of the Aliev–Panfilov model, we first create a pulse of ventricular action potential with a stimulation $I=30$ over an infinite time period $T=\infty$. At 90% repolarization, we measure the duration of the action potential $APD_0=29.2[-]$, see Figure 4 (left). The period of stimulation is then sequentially decreased from $T=500[-]$ to $T \approx APD_0$. For each stimulation period T , we compute the action potential duration of the last pulse. For example, the diagram to the left in Figure 6 depicts the generated impulses of the action potential ϕ and the recovery variable r for $T=80[-]$, i.e. $T/APD_0=2.74$. Observe the decrease in action potential duration in the successive stimulations following the first, which is identical to APD_0 . The plot to the right in Figure 6 summarizes the frequency-dependent decrease of the normalized action potential duration APD/APD_0 with the decrease of the normalized period of stimulation T/APD_0 . These results are in quantitative agreement with the nature of the Aliev–Panfilov model [18] and the behavior of cardiac tissue.

5.2. Excitation of ventricular tissue by pacemaker cells

The first set of initial boundary-value problems is concerned with excitation of ventricular tissue by pacemaker cells. In contrast to the finite difference-based computations reported in the literature, which are restricted to external stimulations, our finite element model can assign distinct cell

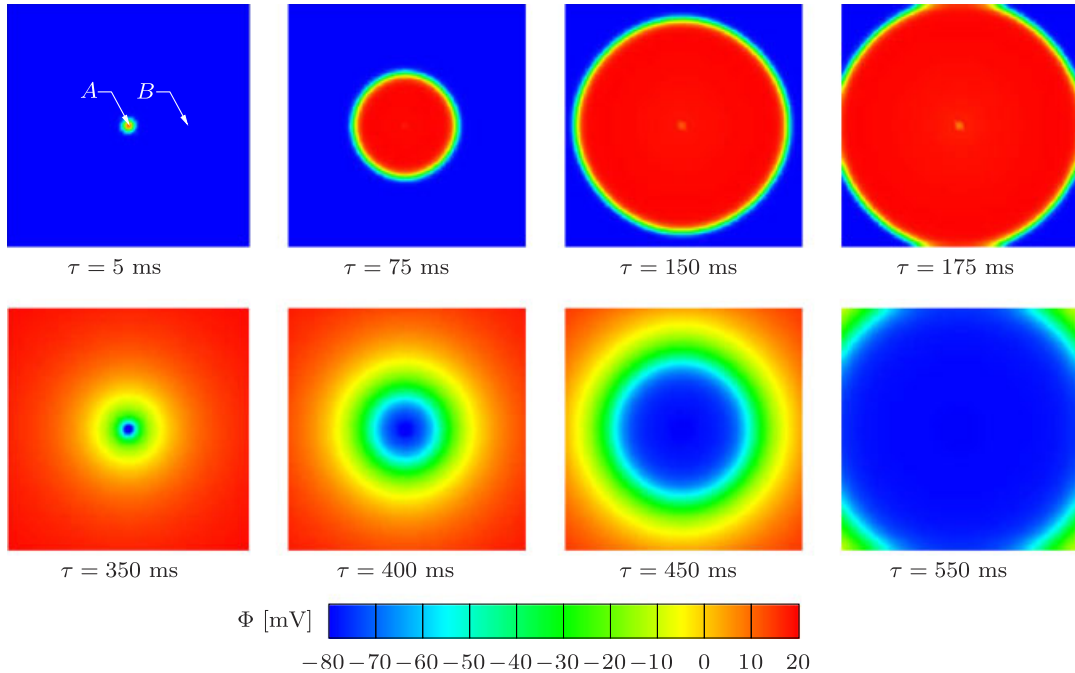


Figure 7. Single central pacemaker element of Fitz–Hugh Nagumo-type exciting the remainder of a square ventricular tissue block of Aliev–Panfilov type through isotropic conduction. Distinct stages of depolarization (upper row) and repolarization (lower row).

properties to different tissue domains. Typical examples are oscillatory FitzHugh–Nagumo-type pacemaker cells, non-oscillatory Aliev–Panfilov-type cardiac muscle cells, fast conduction Purkinje fiber cells, or slow conduction atrioventricular node cells. Here, we consider a $100\text{ mm} \times 100\text{ mm}$ square domain of cardiac tissue discretized into 61×61 four-node quadrilateral elements, see Figure 7. The element in the center (point A) is assigned the self-oscillatory FitzHugh–Nagumo material parameters, the same as the set given in Figure 3. The rest of the tissue is assumed to be made up of ventricular muscle cells modeled by the Aliev–Panfilov model with the material parameters given in Figure 4 except for $\alpha=0.01$. Initial values $\Phi_0^{\text{ap}} = -80\text{ mV}$ are assigned to the nodal action potential values of the ventricular cells. The initial value $\Phi_0^{\text{fn}} = 0\text{ mV}$ is assigned to the nodal action potential degrees of freedom of the central pacemaker element at point A. The conductivity is assumed to be isotropic $\mathbf{D} = d^{\text{iso}}\mathbf{I}$ with $d^{\text{iso}} = 0.1\text{ mm}^2/\text{ms}$, i.e. $d^{\text{ani}} = 0\text{ mm}^2/\text{ms}$. Snapshots of the action potential Φ contour plots taken at different times of computation depict the distinct stages of depolarization, upper row, and repolarization, lower row, of Figure 7. The snapshots taken at $\tau = 175\text{ ms}$ and $\tau = 550\text{ ms}$ nicely verify the zero-flux natural boundary conditions, $\mathbf{q} \cdot \mathbf{n} = 0$, with isolines being oriented orthogonal to the four edges. The contour plots reflect the calcium exchange-induced wide plateau of cardiac muscle cells. As expected from the preceding local analysis of the Aliev–Panfilov model, the contour plots display a much sharper gradient at the wave front than at the wave tail. In addition to the spatial contour plots of the potential field Φ , time variation of the action potential values at the selected points A and B is shown in

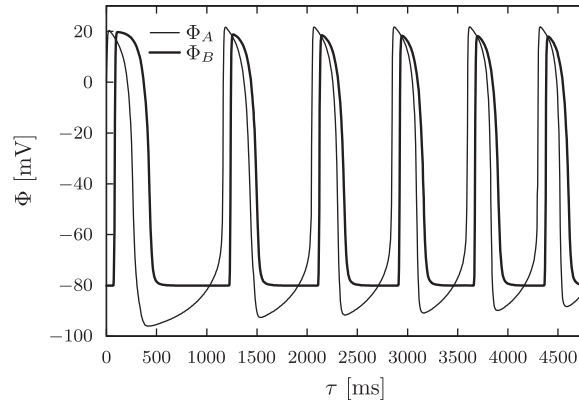


Figure 8. Action potential curves computed for FitzHugh–Nagumo-type pacemaker cell at point A and for Aliev–Panfilov type cardiac muscle cell at point B as depicted in Figure 7. Action potential of cardiac muscle cells displays characteristic restitution property of the Aliev–Panfilov model.

Figure 8 over a longer period of time involving multiple depolarization–polarization cycles. This plot clearly demonstrates not only the distinct shapes of the action potentials of pacemaker cells and cardiac muscle cells, but also illustrates the restitution property of the Aliev–Panfilov model for ventricular muscle cells.

In contrast to the preceding example, in which the conduction tensor \mathbf{D} was assumed to be isotropic, we now analyze the same problem for an anisotropic conduction tensor $\mathbf{D} = d^{\text{iso}}\mathbf{I} + d^{\text{ani}}\mathbf{n} \otimes \mathbf{n}$ with $d^{\text{iso}} = 0.01 \text{ mm}^2/\text{ms}$ and $d^{\text{ani}} = 0.1 \text{ mm}^2/\text{ms}$. The fiber direction of fast conduction \mathbf{n} is assumed to be oriented along the upward diagonal of the square. The contour plots of the action potential Φ in Figure 9 reflect the anisotropic character of the conduction tensor. The circular isopotential lines of the preceding example in Figure 8 are converted to elliptical lines whose long principal axis coincides with the fiber direction \mathbf{n} . Furthermore, we observe more gradual gradients in the fast conducting direction \mathbf{n} compared with the direction perpendicular to it. Apparently, the difference between the gradients is more pronounced during the repolarization phase illustrated in the lower row of Figure 9.

In the last example of this subsection, in addition to the central pacemaker, we consider another pacemaker element near the lower left corner located at 20% of the total length and height of the square domain, i.e. element 11 from the left and bottom edges for the 61×61 mesh, see Figure 10. The conduction tensor is assumed to be purely isotropic $\mathbf{D} = d^{\text{iso}}\mathbf{I}$ with $d^{\text{iso}} = 0.1 \text{ mm}^2/\text{ms}$. The other material parameters are taken to be identical to the ones in the two preceding examples. Compared with the single pacemaker example in Figure 7, two circular depolarization waves are generated in phase. These waves then combine to form a non-convex wave front, see upper row of Figure 10. Analogous interaction between the repolarization waves can be observed, see lower row of Figure 10.

5.3. Spiral wave re-entry

Probably one of the most interesting benchmark problems of computational electrophysiology is the formation of spiral waves that is closely related to re-entrant cardiac arrhythmias and atrial and ventricular fibrillation. The restitution property of the cardiac cell model plays an important role in

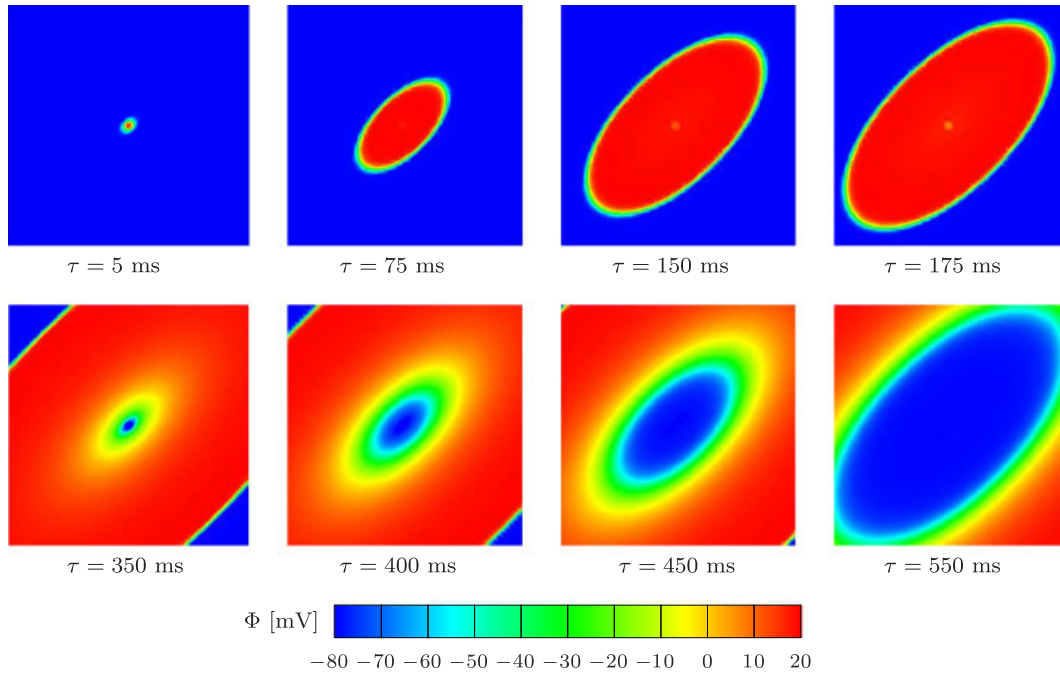


Figure 9. Single central pacemaker element of Fitz–Hugh Nagumo-type exciting the remainder of a square ventricular tissue block of Aliev–Panfilov type through anisotropic conduction with preferred conduction along the upward diagonal. Distinct stages of depolarization (upper row) and repolarization (lower row).

the formation and stable rotation of physiologically realistic spiral waves. Re-entry may result from different inhomogeneities in the cardiac tissue. It might be the uneven distribution of conduction properties in diseased cardiac tissue as in the case of unidirectional block or unsynchronized multiple pacemakers resulting in a spiral wave.

To initiate a spiral wave, we follow the procedure suggested in [18]. We consider a $100\text{mm} \times 100\text{mm}$ block of cardiac tissue discretized into 101×101 four-node quadrilateral elements, see Figure 11. In contrast to the pacemaker examples, this tissue block is now entirely homogeneous consisting of cardiac muscle cells of Aliev–Panfilov type with the same material parameters as in Figure 4 except for $\alpha=0.01$. The conduction tensor is assumed to be isotropic $\mathbf{D}=d^{\text{iso}}\mathbf{I}$ with $d^{\text{iso}}=0.2\text{mm}^2/\text{ms}$. In order to initiate a planar wave in the horizontal direction, the initial values of the nodal action potential on the left vertical edge are set to $\Phi_0=-40\text{mV}$. Once the wave front has formed, it starts to travel in the horizontal direction depolarizing the whole domain, see the panel at $\tau=125\text{ms}$ in Figure 11. The depolarizing wave tail then follows the wave front as shown in the snapshot taken at $\tau=500\text{ms}$. To initiate the spiral wave re-entry, we externally depolarize the rectangular region bounded by the coordinates $x \in [67, 70]\text{mm}$ and $y \in [0, 50]\text{mm}$ with respect to the origin at the lower left corner. The rectangular region is depolarized by stimulating with $I=40$ at time $\tau=570\text{ms}$ for $\Delta t=10\text{ms}$. The panels belonging to the time steps following the stimulation clearly demonstrate the stages of initiation, development, and stable rotation of the spiral wave re-entry. It is important to point out that the duration of the action potential is considerably shortened

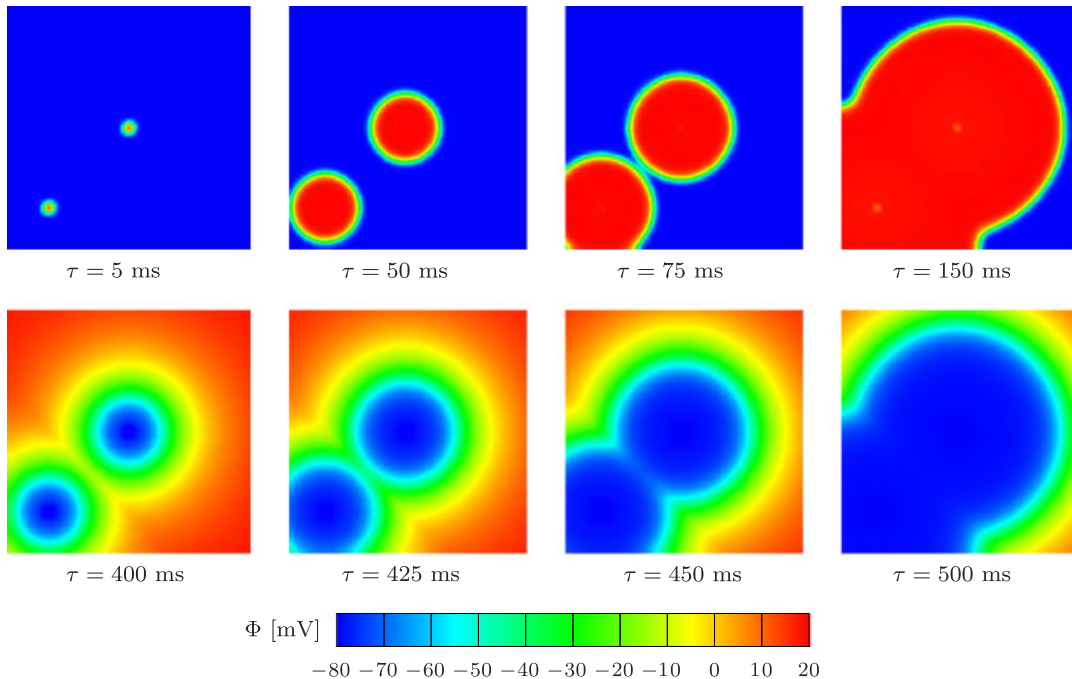


Figure 10. Two interacting pacemaker elements of Fitz–Hugh Nagumo-type exciting the remainder of a square ventricular tissue block of Aliev–Panfilov type through isotropic conduction. Distinct stages of depolarization (upper row) and repolarization (lower row).

as the stable spiral wave is formed, especially as compared with action potential duration of the planar wave shown in the panels at $\tau = 175$ ms and $\tau = 550$ ms in Figures 7 and 9.

5.4. Electroactivity of the heart

The spatio-temporal organization of electrical conduction in myocardial tissue is vital for the synchronized contraction of the heart. The coordinated conduction of electrical waves is achieved by a naturally structured complex cardiac conduction system. The impulse is generated at the heart's natural pacemaker, the sinoatrial node, located in the right atrium. It then travels through the atria, the upper chambers of the heart, and is conducted to the ventricles, the lower chambers via the atrioventricular node. The atrioventricular node is located in the center of the interface between the atria and ventricles. It serves as a unique pathway of conduction from the upper chambers of the heart to its lower chambers. The conduction of the electrical signal is significantly delayed at the atrioventricular node. This delay is crucial to ensure that the blood in the atria is completely ejected into the lower chambers before the ventricles are excited. Once the excitation passes the atrioventricular node, the His bundle takes over and conducts the electrical wave through the septum, the wall between ventricles. The signal first travels to the apex, and then to the right and left ventricular endocardium, the inner walls of the ventricles, through the left and right bundle branches (see Figure 13). The electrical excitation is further transmitted to the ventricular muscle cells by the fast-conducting Purkinje fibers emanating from the bundle branches to the inner parts

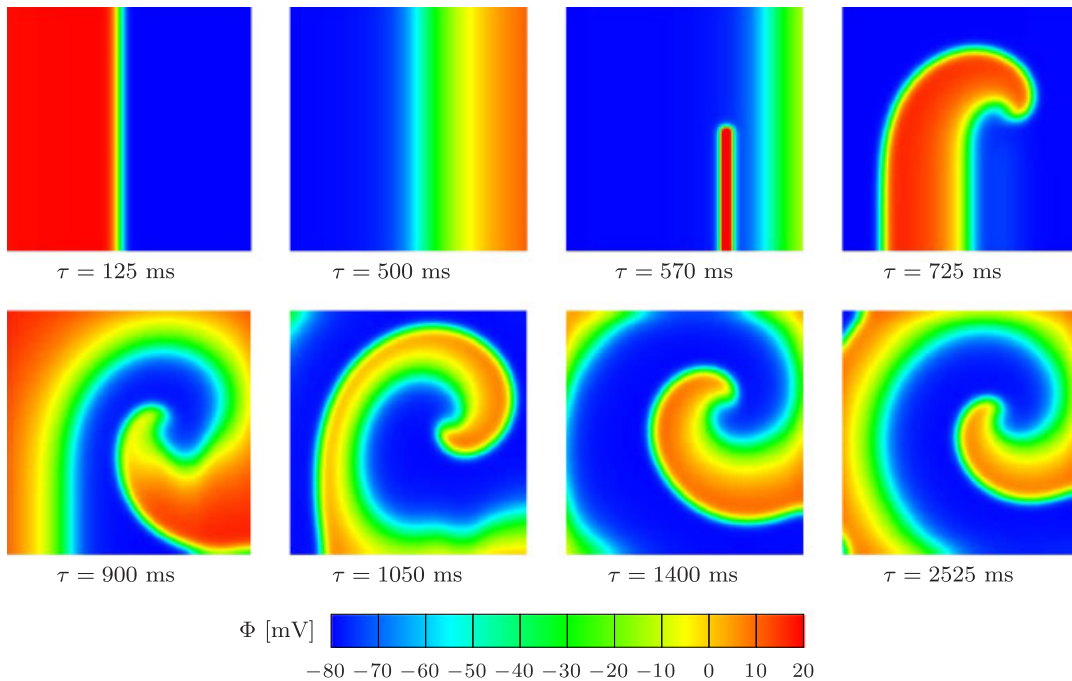


Figure 11. Initiation, development, and rotation of spiral wave re-entry in square block of cardiac muscle tissue. Initiation of planar wave through initial excitation of $\Phi_0 = -40\text{mV}$ at time $\tau = 0\text{ms}$ on left boundary. Initiation of spiral wave through external stimulation of $I = 40$ at time $\tau = 570\text{ms}$ for $\Delta t = 10\text{ms}$ in red domain in third snapshot.

of the myocardium. The physiological excitation times of distinct regions of the heart relative to the His bundle are illustrated in Figure 12 as adopted from Klabunde [6]. The activation delay is a result of different conduction velocities: The conduction velocity in the Purkinje fibers is approximately eight times faster than that of cardiac muscle cells and roughly four times faster than the speed of conduction in the left and right bundles. The delay in the atrioventricular node is the result of its extremely slow conduction rate that is about ten times slower than that of the ventricular muscle tissue [6].

In this final numerical example, we aim at quantitatively predicting the activation times at different locations in the human heart. To this end, we consider a dissection of the real human heart shown in Figure 12 (left). The longitudinal cross-section is discretized into 3525 four-node quadrilateral elements as depicted in Figure 12 (right). We account for two distinct cell types: FitzHugh–Nagumo-type pacemaker cells for the atrioventricular node extension and Aliev–Panfilov-type ventricular muscle cells for the rest of the heart, see Figure 13. The self-oscillatory FitzHugh–Nagumo material parameters of the elements in the atrioventricular node extension are taken to be the same as the set given in Figure 3. The material parameters of the remaining ventricular cells are identical to the ones given in Figure 4 except for $\alpha = 0.01$. In order to trigger the oscillatory pacemaker activity of the atrioventricular node, the initial value $\Phi_0 = 10\text{mV}$ is assigned to the action potential degrees of freedom at its nodes. All ventricular nodes are assigned the resting action potential value of $\Phi_0 = -80\text{mV}$. The outer surface of the dissection is assumed to be flux free, i.e. $\mathbf{q} \cdot \mathbf{n} = 0$. The conduction tensor is assumed to be isotropic $\mathbf{D} = d^{\text{iso}} \mathbf{I}$, but different

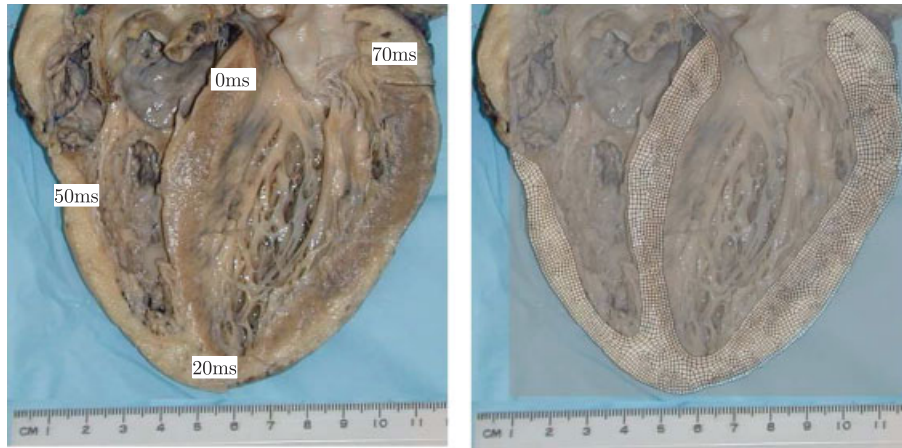


Figure 12. Cross section of human heart with relative excitation times of different regions adopted from [6] (left). Finite element discretization of the dissection with 3525 four-node quadrilateral elements (right).

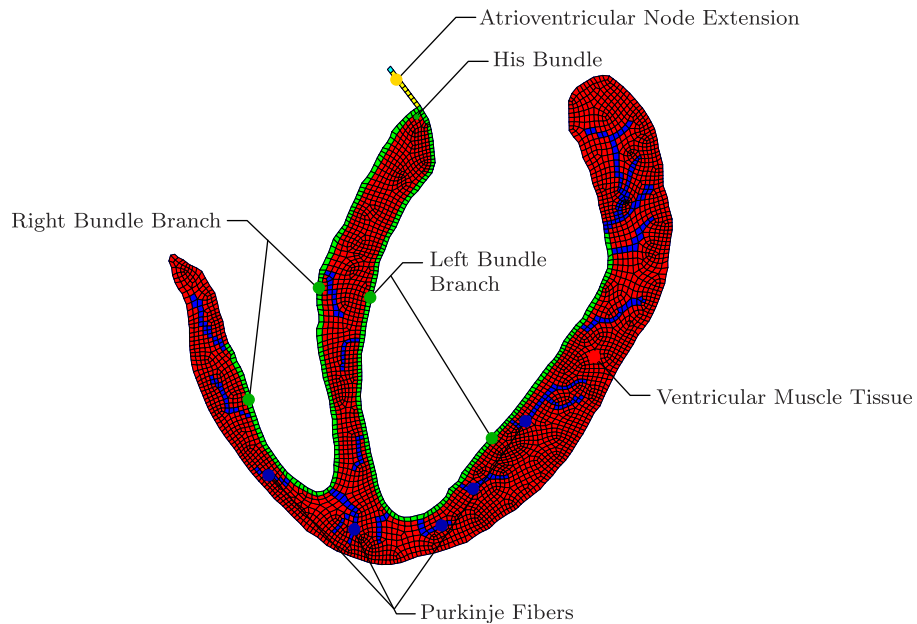


Figure 13. Electrical conduction system of the heart incorporated in the present finite element model. Tissue-specific conductivities of ventricular muscle tissue $d^{\text{mus}} = 10 \text{ mm}^2/\text{ms}$, atrioventricular node extension $d^{\text{avn}} = 1 \text{ mm}^2/\text{ms}$, His bundle and its branches $d^{\text{his}} = 40 \text{ mm}^2/\text{ms}$, and Purkinje fibers $d^{\text{pur}} = 80 \text{ mm}^2/\text{ms}$.

COMPUTATIONAL MODELING OF CARDIAC ELECTROPHYSIOLOGY

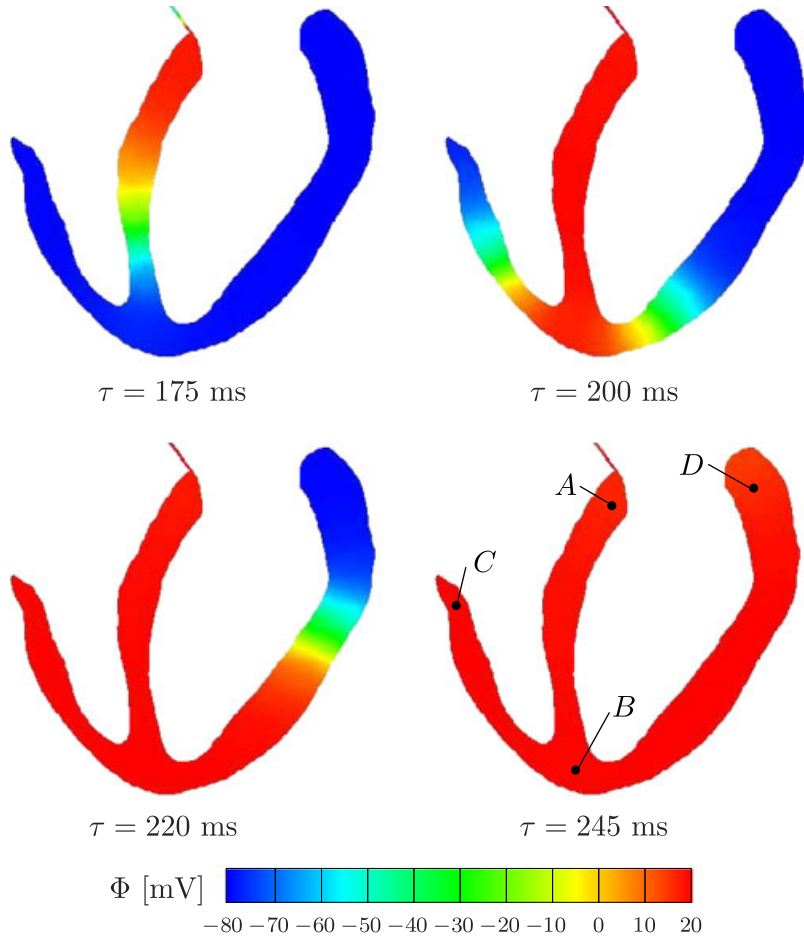


Figure 14. Snapshots of action potential contours at different stages of depolarization: Septal activation through the His bundle at $\tau=175$ ms, activation of anterioseptal region of the ventricular myocardium at $\tau=200$ ms, activation of major portion of ventricular myocardium at $\tau=220$ ms, and late activation of posterobasal portion of the left ventricle and pulmonary conus at $\tau=245$ ms.

cell types are assigned for different isotropic conductivities d^{iso} . The conductivity of the ventricular muscle tissue is assumed to be $d^{mus} = 10 \text{ mm}^2/\text{ms}$ and the coefficients of conductivity of the other cell types are scaled accordingly. Guided by the literature [1], we assume $d^{avn} = 0.1 \times d^{mus}$ for the atrioventricular node extension, $d^{his} = 4 \times d^{mus}$ for the His bundle and its branches, and $d^{pur} = 8 \times d^{mus}$ for the Purkinje fibers. The different spatial locations of the distinct tissue types are depicted in Figure 13.

The contour plots of the action potential at different stages of depolarization are shown in Figure 14. As indicated in Figure 12, points *B*, *C*, and *D* are characterized through an activation delay of 20 ms, 50 ms, and 70 ms with respect to point *A*, see [1, 6]. In the computational simulation, the action potential builds up in the atrioventricular node until approximately $\tau=175$ ms and then spreads out into the ventricular tissue as illustrated in the first snapshot. The second snapshot

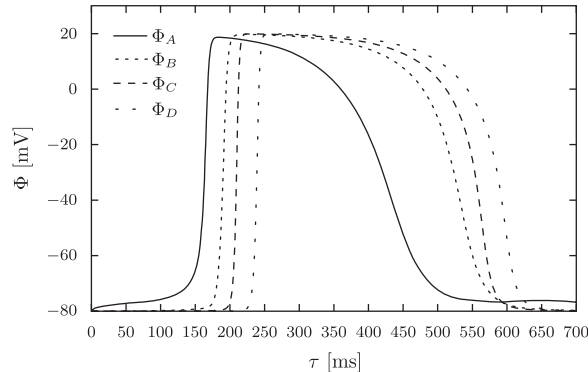


Figure 15. Action potential curves observed at point A in the His bundle with an activation time of $\tau=175$ ms, point B at the apex with an activation time of $\tau=200$ ms, point C in the upper right ventricle with an activation time of $\tau=220$ ms, and point D in the upper left ventricle an activation time of $\tau=245$ ms, compare Figure 14.

is taken 25 ms later and thus corresponds favorably to the 20 ms activation delay in the apex. After 45 ms, the excitation signal has reached the upper right ventricle as illustrated in the third snapshot. The last snapshot shows the excitation of the outermost cells of the left ventricle with a 75 ms delay. Again, this value agrees favorably with the 70 ms activation delay reported in the literature. To complement the contour plots, we illustrate the action potential curves at nodes A , B , C , and D in Figure 15. The activation times demonstrate that the proposed model quantitatively captures the correct excitation sequence. Last, in addition to the potential values, we also plot the norm of the potential gradient contours in Figure 16. These contour plots at different stages of depolarization clearly show the underlying well-organized conduction system with a fast-spreading signal along the Purkinje fibers. The complex cardiac conduction system is realistically captured by the proposed model.

6. DISCUSSION

For the first time, we have derived a modular finite element formulation for electrophysiology and demonstrated its potential in simulating well-documented excitation scenarios and a patient-specific excited human heart. In contrast to the finite difference schemes and collocation methods proposed in the literature, this new framework is (i) unconditionally stable; (ii) extremely efficient; (iii) highly modular; (iv) geometrically flexible; and (iv) easily expandable. Unconditional stability is guaranteed by using an implicit Euler backward time integration procedure instead of the previously used explicit schemes. This procedure is extremely robust, in particular in combination with an incremental iterative Newton–Raphson solution technique. Efficiency is introduced through the implicit time integration, which enables the use of significantly larger time steps than explicit schemes. Our particular global–local split additionally contributes to the efficiency of the proposed scheme, since we only introduce a single degree of freedom at each finite element node. Modularity originates from the particular discretization scheme that treats all unknowns except for the globally introduced action potential as local internal variables on the integration point level. Accordingly,

COMPUTATIONAL MODELING OF CARDIAC ELECTROPHYSIOLOGY

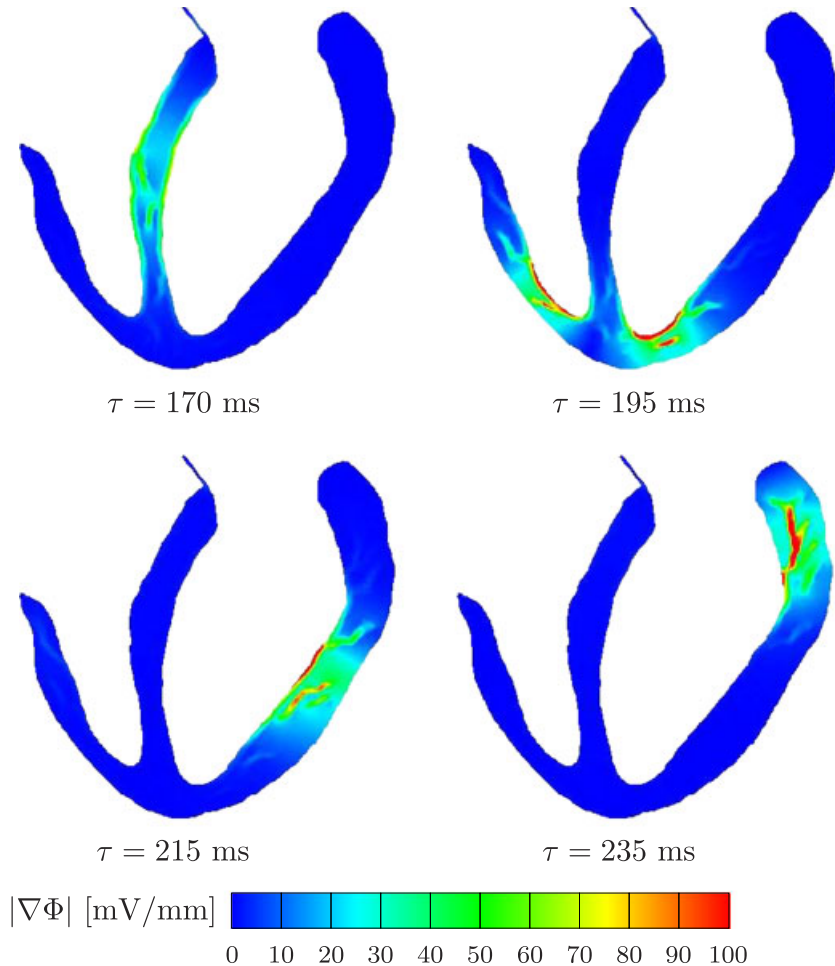


Figure 16. Snapshots of norm of action potential gradient contours at different times stages of depolarization. Fast distribution of electrical signal through Purkinje fiber conduction system. Activation of ventricular myocardium from endocardial surfaces.

not only the suggested two parameter FitzHugh–Nagumo model [9] and the Aliev–Panfilov model [18], but also the more sophisticated Hodgkin–Huxley model, the Noble model [10], the Beeler–Reuter model [11], the Luo–Rudy model [12], the Fenton–Karma model [19] and many others can be incorporated in this general framework by simply adding new constitutive modules and adjusting the number of internal variables per integration point. Different models for different cell types can be combined straightforwardly allowing for a fully inhomogeneous description of the underlying tissue microstructure. In contrast to the literature, all our examples were self excited by using oscillatory pacemaker cells in combination with non-oscillatory muscle cells. In principle, our discretization scheme allows for individual adaptive time-stepping schemes for the fast and slow variables. Unlike existing schemes that are most powerful on regular grids, the proposed

finite element-based excitation framework can be applied to arbitrary geometries with arbitrary initial and boundary conditions.

The most important feature of the proposed algorithm, however, is that it lays the groundwork for a robust and stable whole heart model of excitation–contraction coupling. Through a straightforward generalization, the proposed excitation algorithm can be coupled to cardiac contraction through the additional incorporation of the mechanical deformation field. Traditionally, the electrical problem has been solved with finite difference schemes with a high spatial and temporal resolution. After several electrical time steps, the electric potential was mapped onto a coarse grid to solve the mechanical problem with finite element methods and map the resulting deformation back to the smaller grid. Spatial mapping errors and temporal energy blow up are inherent to this type of solution procedure. We are currently working on a fully coupled monolithic solution of the electro-mechanical problem for excitation–contraction that simultaneously solves for the electrical potential and for the mechanical deformation in a unique, robust, and efficient way. This framework can potentially be applied to explain, predict, and prevent rhythm disturbances in the heart. A typical application is biventricular pacing [32, 33], a promising novel technique in which both the left and right ventricle are stimulated externally to induce cardiac resynchronization after heart failure.

ACKNOWLEDGEMENTS

The authors would like to thank Chengpei Xu, MD, PhD, for providing cross-sections of the human heart, Oscar Abilez, MD, and Wolfgang Bothe, MD, for valuable input to the manuscript, and all members of the Cardiovascular Tissue Engineering Group at Stanford for various stimulating discussions. This material is based on work supported by the National Science Foundation under Grant No. EFRI-CBE 0735551 ‘Engineering of cardiovascular cellular interfaces and tissue constructs’. Any opinions, findings and conclusions or recommendations expressed in this material are those of the authors and do not necessarily reflect the views of the National Science Foundation.

REFERENCES

1. Ganong WF. *Review of Medical Physiology*. McGraw-Hill, Appleton & Lange: New York, 2003.
2. Berne RM, Levy MN. *Cardiovascular Physiology*. The Mosby Monograph Series. Mosby Inc.: St. Louis, 2001.
3. Bers MD. *Excitation-contraction Coupling and Cardiac Contractile Force*. Kluwer Academic Publishers: Dordrecht, 2001.
4. Durrer D, van Dam T, Freud E, Janse MJ, Meijlers FL, Arzbaeher RC. Total excitation of the isolated heart. *Circulation* 1970; **41**:899–912.
5. Opie LH. *Heart Physiology: From Cell to Circulation*. Lippincott Williams & Wilkins: Philadelphia, 2003.
6. Klabunde RE. *Cardiovascular Physiology Concepts*. Lippincott Williams & Wilkins: Philadelphia, 2005.
7. Plonsey R, Barr RC. *Bioelectricity. A Quantitative Approach*. Springer Science and Business Media: New York, 2007.
8. Hodgkin AL, Huxley AF. A quantitative description of membrane current and its application to conductance and excitation in nerve. *Journal of Physiology* 1952; **117**:500–544.
9. FitzHugh R. Impulses and physiological states in theoretical models of nerve membranes. *Biophysical Journal* 1961; **1**:445–466.
10. Noble D. A modification of the Hodgkin–Huxley equations applicable to Purkinje fibre action and pacemaker potentials. *Journal of Physiology* 1962; **160**:317–352.
11. Beeler GW, Reuter H. Reconstruction of the action potential of ventricular myocardial fibers. *Journal of Physiology* 1977; **268**:177–210.
12. Luo C, Rudy Y. A model of the ventricular cardiac action potential. Depolarization, repolarization, and their changes. *Circulation Research* 1991; **68**:1501–1526.
13. Keener J, Sneyd J. *Mathematical Physiology*. Springer Science and Business Media: New York, 2004.

COMPUTATIONAL MODELING OF CARDIAC ELECTROPHYSIOLOGY

14. Sachse FB. *Computational Cardiology*. Springer: Berlin, 2004.
15. Clayton RH, Panfilov AV. A guide to modelling cardiac electrical activity in anatomically detailed ventricles. *Progress in Biophysics and Molecular Biology* 2008; **96**:19–43.
16. ten Tuschler KHJ, Panfilov AV. Modelling of the ventricular conduction system. *Progress in Biophysics and Molecular Biology* 2008; **96**:152–170.
17. Fenton FH, Cherry EM, Hastings HM, Evans SJ. Multiple mechanisms of spiral wave breakup in a model of cardiac electrical activity. *Chaos* 2002; **12**:852–892.
18. Aliev RR, Panfilov AV. A simple two-variable model of cardiac excitation. *Chaos, Solitons and Fractals* 1996; **7**:293–301.
19. Fenton FH, Karma A. Vortex dynamics in three-dimensional continuous myocardium with fiber rotation: filament instability and fibrillation. *Chaos* 1998; **8**:20–47.
20. Rogers JM, McCulloch AD. A collocation-Galerkin finite element model of cardiac action potential propagation. *IEEE Transactions on Biomedical Engineering* 1994; **41**:743–757.
21. Rogers JM, McCulloch AD. Nonuniform muscle fiber orientation causes spiral wave drift in a finite element model of cardiac action potential propagation. *Journal of Cardiovascular Electrophysiology* 1994; **5**:496–509.
22. Rogers JM. Wave front fragmentation due to ventricular geometry in a model of the rabbit heart. *Chaos* 2002; **12**:779–787.
23. Hunter PJ, McCulloch AD, ter Keurs HEDJ. Modelling the mechanical properties of cardiac muscle. *Progress in Biophysics and Molecular Biology* 1998; **69**:289–331.
24. Nash MP, Panfilov AV. Electromechanical model of excitable tissue to study reentrant cardiac arrhythmias. *Progress in Biophysics and Molecular Biology* 2004; **85**:501–522.
25. Panfilov AV, Nash MP. Self-organized pacemakers in a coupled reaction–diffusion–mechanics system. *Physical Review Letters* 2005; **95**:258104:1–4.
26. Nickerson D, Nash M, Nielsen P, Smith N, Hunter P. Computational multiscale modeling in the IUPS physiome project: modeling cardiac electromechanics. *IBM Journal of Research and Development* 2006; **50**:617–630.
27. Keldermann RH, Nash MP, Panfilov AV. Pacemakers in a reaction–diffusion mechanics system. *Journal of Statistical Physics* 2007; **128**:375–392.
28. Panfilov AV, Keldermann RH, Nash MP. Drift and breakup of spiral waves in reaction–diffusion–mechanics systems. *Proceedings of the National Academy of Sciences* 2007; **104**:7922–7926.
29. Tomlinson KA, Hunter P, Pullan AJ. A finite element method for an Eikonal equation model of myocardial excitation wavefront propagation. *SIAM Journal on Applied Mathematics* 2002; **63**:324–350.
30. van der Pol B. On relaxation oscillations. *Philosophical Magazine* 1926; **2**:978–992.
31. Nagumo J, Arimoto S, Yoshizawa S. Active pulse transmission line simulating nerve axon. *Proceedings of the Institute of Radio Engineers* 1962; **50**:2061–2070.
32. Gould PA, Mariani JA, Kaye DM. Biventricular pacing in heart failure: a review. *Expert Review of Cardiovascular Therapy* 2006; **4**:97–109.
33. Hawkins DM, Petrie MC, MacDonald MR, Hogg KJ, McMurray JJV. Selecting patients for cardiac resynchronization therapy: electrical or mechanical dyssynchronization. *European Heart Journal* 2006; **27**:1270–1281.